In-beam measurement of the hydrogen hyperfine splitting - towards antihydrogen spectroscopy

M. Diermaier,[1] C. B. Jepsen,[2,*] B. Kolbinger,[1] C. Malbrunot,[2,1]
O. Massiczek,[1] C. Sauerzopf,[1] M. C. Simon,[1] J. Zmeskal,[1] and E. Widmann[1,†]

[1] *Stefan-Meyer-Institut für Subatomare Physik, Österreichische Akademie der Wissenschaften, Wien 1090, Austria*
[2] *CERN, Genève 1211, Switzerland*

Antihydrogen, the lightest atom consisting purely of antimatter, is an ideal laboratory to study the $\mathcal{CPT}$ symmetry by comparison to hydrogen. With respect to absolute precision, transitions within the ground-state hyperfine structure (GS-HFS) are most appealing by virtue of their small energy separation. ASACUSA proposed employing a beam of cold antihydrogen atoms in a Rabi-type experiment to determine the GS-HFS in a field-free region. Here we present a measurement of the zero-field hydrogen GS-HFS using the spectroscopy apparatus of ASACUSA's antihydrogen experiment. The measured value of ν_{HF}=1 420 405 748.4(3.4)(1.6) Hz with a relative precision of $\Delta\nu_{\mathrm{HF}}/\nu_{\mathrm{HF}}=2.7\times10^{-9}$ constitutes the most precise determination of this quantity in a beam and verifies the developed spectroscopy methods for the antihydrogen HFS experiment to the ppb level. Together with the recently presented observation of antihydrogen atoms 2.7 m downstream of the production region, the prerequisites for a measurement with antihydrogen are now available within the ASACUSA collaboration.

Investigations of the hydrogen atom have been a driving force for the discovery of more profound theories [1] and contribute to the basis of physics through their prominent influence on the definition of fundamental constants [2]. Most notable from a precision point of view are the recent measurement of the $1S-2S$ transition via two-photon spectroscopy [3] and the determination of the hyperfine splitting in hydrogen maser experiments in the early 1970s [4–9]. The achieved absolute (relative) precisions are 10 Hz (4×10^{-15}) and 2 mHz (1.4×10^{-12}), respectively. A revival of the interest in hydrogen is founded on prospects of antihydrogen ($\overline{\mathrm{H}}$) research [10, 11]. The structure of the simplest antiatom, consisting of a positron bound to an antiproton is predicted to be identical to that of hydrogen, if the combined symmetry of charge conjugation, parity, and time reversal ($\mathcal{CPT}$) is conserved. Hence, antihydrogen spectroscopy promises precise tests of the $\mathcal{CPT}$ symmetry, which is a cornerstone of the Standard Model of particle physics. A vivid physics program is currently underway at the Antiproton Decelerator of CERN aiming at spectroscopic [12–16] and gravity tests [17, 18] along with other $\mathcal{CPT}$ tests like the neutrality of antihydrogen [19, 20] as well as measurements of the charge-to-mass ratio [21] and magnetic moment [22] of the antiproton.

Among the spectroscopic tests of $\mathcal{CPT}$, the comparison of the GS-HFS of hydrogen and antihydrogen has the potential to reach the highest sensitivity on an absolute energy scale [23–25]. However, the aforementioned most precise measurement of this quantity for hydrogen was made using a maser [8]. Such a technique is not applicable to antimatter which would annihilate with the confining matter enclosure. The measurement proposed by the ASACUSA collaboration at the Antiproton Decelerator of CERN therefore makes use of a beam of cold antihydrogen atoms [26, 27]. In addition to avoiding wall interaction, the actual measurement takes place in a field-free region, ultimately allowing for higher precision compared to the observation of resonant quantum transitions between the hyperfine states in trapped antihydrogen in a high-field environment [28].

Rabi-type magnetic resonance spectroscopy [29, 30] applies rotating (or oscillating) magnetic fields to induce quantum transitions and exploits the force of magnetic field gradients on the state-dependent magnetic moment of atoms (or molecules) in order to spatially separate the atoms in a beam with respect to their quantum states (Stern-Gerlach separation). Typically magnetic sextupole fields are employed to focus atoms in low-field-seeking states (*lfs*) and defocus high-field-seekers (*hfs*). In the case of ground-state hydrogen the hyperfine structure consists of a lower lying singlet state with total angular momentum quantum number F=0 ($\mathbf{F}=\mathbf{S}^p+\mathbf{S}^e$ with $\mathbf{S}^p$ and $\mathbf{S}^e$ being proton and electron spin, respectively) and a triplet state F=1. As illustrated by the Breit-Rabi diagram in Fig. 1 the triplet state degeneracy is lifted in the presence of a magnetic field. The singlet state and the triplet state with magnetic quantum number $M_{\mathrm{F}}=-1$ are *hfs*, while the other two states (F=1, M_{F}=0,1) are *lfs*. In the present experiment the σ_1-transition from (F=1, M_{F}=0) to (F=0, M_{F}=0) has been studied [31, 32]. The Zeeman-shifted frequencies at various external magnetic field strengths were determined for subsequent

* Present address: Department of Physics
Princeton University, New Jersey 08544, USA
† eberhard.widmann@oeaw.ac.at

extraction of the zero-field value and resulted in

$$\nu_{\rm HF} = 1\ 420\ 405\ 748.4(3.4)(1.6)\,{\rm Hz}. \qquad (1)$$

The numbers in brackets are the one standard deviation (1σ) statistical and systematic uncertainties. Added in quadrature the total uncertainty of 3.8 Hz constitutes an improvement by more than an order of magnitude in comparison to the previously achieved best precision by Rabi-type spectroscopy of 50 Hz [33, 34]. Our result is in agreement within one standard deviation with the literature value of $\nu_{\rm lit}$=1 420 405 751.768 (2) Hz, which relies on the more precise hydrogen maser measurements [4] (see discussion in §6 of [5]).

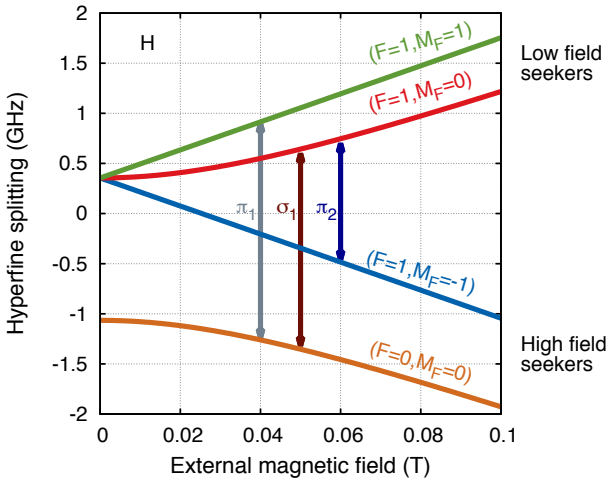

Figure 1. ***Ground state hyperfine splitting in hydrogen.*** *The Breit-Rabi diagram shows the energy levels in ground-state hydrogen as a function of the strength of an external magnetic field. The 4 hyperfine states separate into a singlet state and a triplet state, which exhibit different Zeeman shifts. The states with a positive or negative slope are named low or high field seekers, respectively. Three possible hyperfine transitions between lfs and hfs are denoted by arrows, the σ_1-transition occurs between the states (F=1,M_F=0) and (F=0,M_F=0).*

I. RESULTS

A. Experimental Setup

The main components of the experiment are a source of cooled and polarized atomic hydrogen, the hyperfine spectrometer of the $\overline{\rm H}$ hyperfine splitting (HFS) setup (i.e. a microwave cavity and a superconducting sextupole magnet), and a hydrogen detector (cf. Fig. 2). The atomic hydrogen source maintains a microwave driven plasma in a pyrex cylinder to dissociate molecular hydrogen ($H_2 \rightarrow H + H$) [35]. Hydrogen atoms are allowed into the first vacuum chamber through a PTFE tubing, which is kept under cryogenic temperatures in order to cool the hydrogen atoms and hence reduce their velocity [36]. Two tubing configurations are used in which the plasma-containing pyrex cylinder is either mounted perpendicular to or on axis with the beam. In the first case, a 90° bent tubing assures an efficient and complete interaction of the hydrogen atoms with the cold PTFE surface. In the latter case, a straight tubing keeps the recombinations caused by wall interactions down to a minimum. The cooled atomic hydrogen beam is directed onto a skimmer of 1 mm in diameter and reaches the second, differentially-pumped chamber, which houses two permanent sextupole magnets with a pole field of ∼1.3 T at a radius of 5 mm over a mechanical length of 65 mm each [37]. In addition to providing the initial spin-polarisation, those sextupole magnets are moveable and feature a midway aperture (aperture 1) to allow for the adjustable selection of a narrow velocity range. As the focusing length depends on the beam velocity, only a certain velocity component is focused onto the aperture and can pass, while the off-axis portions of all other components are blocked. The variable distance to the aperture located at half the distance between the sextuple magnets ($d_{\rm s}$) therefore selects a velocity component. The resulting velocity distribution is much narrower than a Maxwell-Boltzmann distribution and roughly of Gaussian shape. The spin-polarised and velocity-selected hydrogen beam passes another aperture (aperture 2) and is then modulated by a tuning fork chopper in the next differentially-pumped section. The modulation adds time-of-flight measurements to the beam diagnostic tools as well as suppression of background originating from residual hydrogen via lock-in amplification. Downstream of the chopper, apertures of different diameters (aperture 3) can be installed in order to produce different beam sizes at the entrance of the microwave cavity.

The $\overline{\rm H}$ HFS spectrometer has been designed with an open diameter of 100 mm since a large acceptance is crucial in view of small $\overline{\rm H}$ production rates. The amplitude of the oscillating magnetic field $B_{\rm osc}$ has to be sufficiently uniform over the large open diameter in order to guarantee a trajectory-independent state-conversion probability. This requirement is best met by a cavity of so-called strip-line geometry [38, 39]. Two highly transparent meshes confine the microwaves at the entrance and exit of the state-conversion cavity, which are separated by half a wavelength of the hyperfine splitting transition ($L_{\rm cav} \sim \lambda_{HF}/2 \sim 105.5$ mm). A standing wave forms between them and as a consequence $B_{\rm osc}$ is not constant along

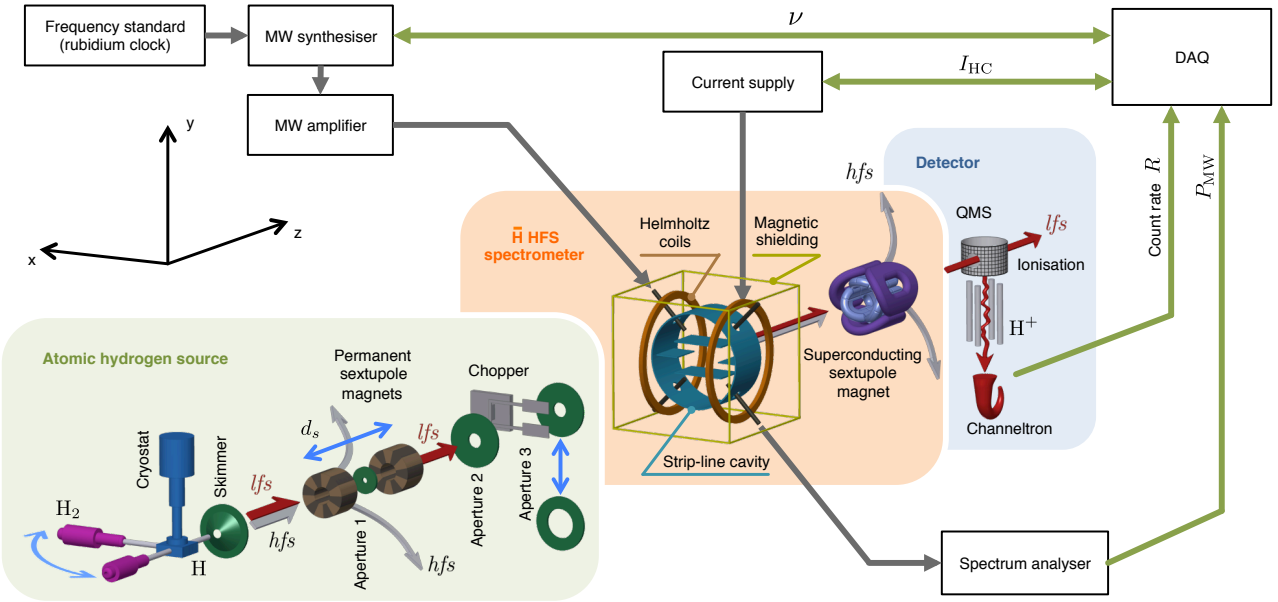

Figure 2. ***Atomic hydrogen beam setup.*** *Illustration of the three main components of the Rabi-type experimental setup (not to scale). Green panel: the source of cold, polarised, and modulated atomic hydrogen. Orange panel: the hyperfine spectrometer of ASACUSA's antihydrogen experiment. Blue panel: the detector. The source consists of a microwave driven plasma for dissociation of H_2, a cryostat for cooling the atomic hydrogen beam in a PTFE tubing, two permanent sextupole magnets for polarisation and velocity selection, and a tuning fork chopper for beam modulation. The hyperfine spectrometer consists of a state-conversion cavity of strip-line geometry and Helmholtz coils enclosed in a cuboidal Mu-metal shielding followed by a superconducting sextupole magnet for spin-state analysis. The detector employs a quadrupole mass spectrometer for selective mass=1 ion (H^+) counting after ionisation. The count rate is acquired as a function of the driving frequency supplied to the cavity.*

the beam propagation direction, causing a *double-dip* resonance line-shape. The origin of this structure is outlined below and explained in detail in the Methods. The cavity length and the beam velocity v_H define the interaction time of the hydrogen atoms with the microwave field $T_{\rm int} = L_{\rm cav}/v_H$ and restrict the achievable resonance line width to $\sim T_{\rm int}^{-1}$. A synthesiser coupled to an external rubidium clock for frequency stabilisation produces microwaves, which are fed radially to the cavity via an antenna after amplification. On the opposite side of the cavity another antenna is used for pick-up and monitoring of the microwave power ($P_{\rm MW} \propto B_{\rm osc}^2$) using a spectrum analyser. Helmholtz coils are mounted onto the cavity to generate a homogeneous external magnetostatic field $B_{\rm stat}$, parallel to $B_{\rm osc}$, and of several Gauss in magnitude at the interaction region for fine control of the Zeeman splitting. A current source with a relative stability of 20 ppm supplies the Helmholtz coils' current $I_{\rm HC}$, which is independently monitored by an amperemeter. $I_{\rm HC}$ is directly proportional to $B_{\rm stat}$ and turned out to be a better proxy for the magnetic field inside the cavity than a dedicated external magnetic field measurement. The microwave cavity and the Helmholtz coils are surrounded by a two-layer cuboidal Mu-metal shielding to block the Earth's magnetic field as well as the fringe field of the closely succeeding superconducting sextupole magnet. Owing to the pole strength of up to 3.5 T, this magnet generates sizeable magnetic field gradients despite the large open diameter of 100 mm. The integrated gradient amounts to 150 T/m and ensures refocusing of 50 K *lfs* atoms within a distance of ∼1 m.

The detection of hydrogen suffers from a large background rate and small efficiencies. A crossed-beam quadrupole mass spectrometer (QMS) with a 3 mm opening ionises beam atoms and residual gas by electron impact and selectively guides protons to a channeltron for efficient single mass=1 ion counting. The QMS can be moved two-dimensionally in the plane perpendicular to the beam for optimising count rates and investigating beam profiles. Ultrahigh vacuum conditions ($p \leq 5{\times}10^{-10}$ mbar), achieved by combining two-stage turbo-molecular pumping and non-evaporable-getter pumps, lead to count rates of tens of kHz at the QMS for a typical H_2-flowrate of $1.8{\times}10^{17}\,{\rm s}^{-1}$.

B. Measurement procedure

The dissociation plasma was operated under stable standard conditions. Before starting frequency scans the microwave power P_{MW} supplied to the cavity was adjusted to yield the largest state-conversion probability by observing a Rabi oscillation. A single measurement *cycle* was obtained by scanning the frequency once in a random sequence across the desired range. Typically, this included 39 frequency points distributed over ∼40 kHz. At each frequency point the channeltron events of the QMS were summed several times for typical intervals of 5-60 s from which an average count rate was retrieved. Such *cycles* over the frequency range were repeated on average 5 times with changing random sequences to result in a complete *scan* at a given I_{HC}. This was repeated at different values and polarity of I_{HC} to yield a *set* of *scans* suitable for determination of the field-free hyperfine splitting. The number of I_{HC} values per *set* ranged from 6 to 16. In total 10 such *sets* have been recorded, which differ in various of the experimental settings and arrangements (cf. table II).

C. Raw data corrections

Initially a fit as described below was applied to the detected count rates. Two systematic effects were identified in the residuals and corrected for. The first correction compensates slow time drifts. The second correction concerns a type of *memory-effect*, which became evident in an increased likelihood of observing positive or negative residuals if the previous data point was taken at higher or lower count rate, respectively. This indicated, that the settling of the hydrogen rate in the detection chamber following a change of the excitation frequency had a non-negligible time constant when compared to measurement time at each frequency step. These two effects were corrected for at the raw data level and led to an improvement of the fit quality without affecting the extracted ν_{HF} values. The application of a random sequence of frequencies in the *cycles* seemed to suppress systematic impacts of the drift and the memory-effect below the statistical sensitivity.

D. Analysis

The *central frequency* ν_c was extracted from every *cycle* by a fit to the spectrum as illustrated in Fig. 3a, where the excitation frequency ν is given as the difference to ν_{lit}. The *double-dip* line shape originates from the sinusoidal dependence of B_{osc} along the beam axis, which follows half a cosine period. At the actual transition frequency the highest count rate

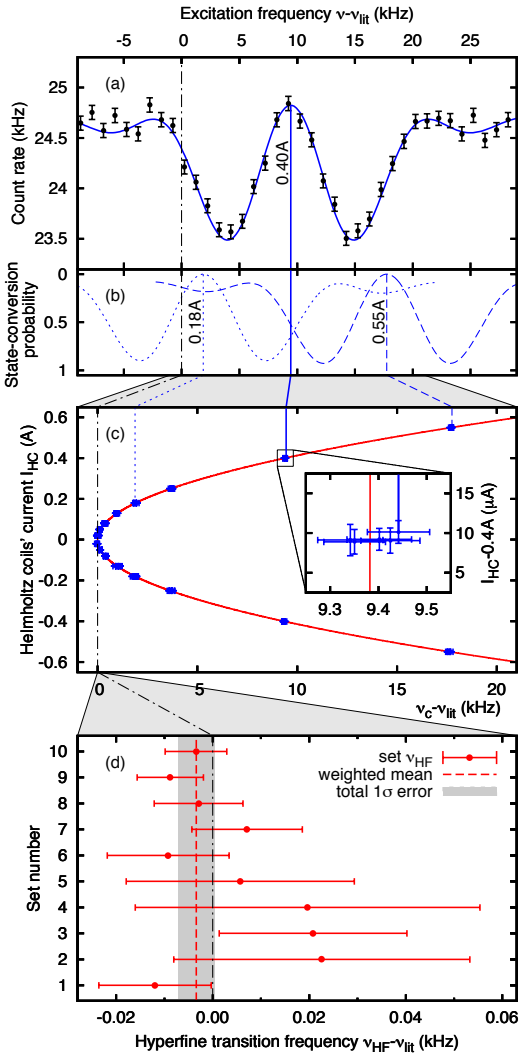

Figure 3. ***Resonance spectrum and zero-field value extraction.*** *(a) Data of one* cycle *of* set *8 at a Helmholtz coils' current I_{HC}=400 mA fitted with the resonance curve ($\mathcal{F}_R$, full blue line, see equation (11) in Methods) to extract the* central frequency ν_c*, which is Zeeman-shifted to values > ν_{HF}. A dashed-dotted black line at 0 is drawn through all the plots to represent ν_{lit}. (b) State-conversion probabilities ($\mathcal{F}$) as obtained from the fit ($\mathcal{F}_R$) of two other* cycles *of the same* set*, but at different settings of I_{HC} (dotted blue line 180 mA, dashed blue line 550 mA, data omitted for clarity). (c) ν_c of all 80* cycles *of* set *8 (16 different values of I_{HC}, 5* cycles *each) plotted against I_{HC} for extraction of the zero-field hyperfine splitting ν_{HF} using the Breit-Rabi fit function ν'_σ (red line) of equation (4). The inset is a zoom into the group of 5* cycles *at I_{HC}=400 mA illustrating the typical size of the frequency and current standard deviations of each data point. (d) The resulting ν_{HF} as deviation from ν_{lit} for the 10* sets *(red error bars) and their weighted mean value (dashed red line) with the 1σ total uncertainty as grey-shaded area.*

between the two dips is observed. The theoretical line shape for a mono-energetic beam is well understood and accurately described within the framework of the two-level system with the interaction Hamiltonian

$$\hat{\mathcal{H}}_{\mathrm{int}} = -\hat{\boldsymbol{\mu}} \cdot \mathbf{B}_{\mathrm{osc}}(t), \tag{2}$$

where $\hat{\boldsymbol{\mu}}$ is the magnetic moment operator as defined in equation (7). The time dependence of the magnetic field includes a $\cos(\pi t/T_{\mathrm{int}})$-term in addition to the microwave oscillations. The resulting equations were solved numerically to obtain the state-conversion probability as a function of the frequency ν and amplitude B_{osc} of the driving field for a mono-energetic beam. A realistic fit function $\mathcal{F}$ for the measured state-conversion probabilities was obtained by convolution of the shape for mono-energetic beams with a velocity distribution as described in the Methods. Consequently, the fit function could extract the physical parameters B_{osc}, the mean velocity of the polarised atomic hydrogen beam $\bar{v}_H$, and the width of the velocity distribution σ_v in addition to ν_c of the transition. Two further fit parameters of less relevant physical content scaled the state-conversion probability to the count rate and correspond to the count rate baseline R_0 and the count rate drop ΔR for complete state conversion. In the final analysis only ν_c was extracted from every *cycle* individually. For B_{osc} a relation to the monitored microwave power was established based on the complete available data. This enabled individual fixation of this parameter for every *set* and avoided non-converging fits due to a strong correlation of B_{osc} with ΔR. For $\bar{v}_H$ and σ_v a common fit value for a complete *set* was used, as all settings of direct impact on the beam velocity remained unchanged during data collection of a *set*.

As illustrated in Fig. 3a the line shape thus obtained resulted in good fits to the observed count rates at all I_{HC} settings with reduced χ^2 values close to unity as summarized in table II. The reliability of the fit function was important since ν_c could be extracted with typical statistical uncertainties on the order of tens of Hz while the width of the *double-dip* structure is on the order of tens of kHz. In Fig. 3c, the extracted ν_c value of each *cycle* of *set* 8 are plotted against the Helmholtz coils' current I_{HC} at which it was recorded. The Zeeman-shifted frequency of the σ_1-transition $\nu_\sigma(B_{\mathrm{stat}})$ has only a second order dependence on the static external magnetic field B_{stat} as apparent from the Breit-Rabi diagram (Fig. 1) and described by the Breit-Rabi formula [40]

$$\nu_\sigma(B_{\mathrm{stat}}) = \sqrt{\nu_{\mathrm{HF}}^2 + \left(\frac{\mu_+}{h}\right)^2 B_{\mathrm{stat}}^2}, \qquad \mu_+ = |g_e|\mu_B + g_p\mu_N, \tag{3}$$

with μ_B=5.788 381 8012×10^{-5} eVT^{-1} and μ_N=3.152 451 2550×10^{-8} eVT^{-1} being respectively the Bohr and nuclear magneton, g_e=-2.002 319 304 361 82 and g_p=5.585 694 702 [2] being respectively the g-factors of the electron and proton, and h=2$\pi\hbar$ the Planck constant. In order to extract the zero-field hyperfine transition frequency ν_{HF} a fit function ν'_σ was required, that used I_{HC} as a variable. A factor k converting I_{HC} to a magnetic field and a residual field B_{res} at $I_{\mathrm{HC}} = 0$ added two further fit parameters and established a linear relation to B_{stat}, which enters the Breit-Rabi formula

$$\nu'_\sigma(I_{\mathrm{HC}};\nu_{\mathrm{HF}},k,B_{res}) = \sqrt{\nu_{\mathrm{HF}}^2 + \left(\frac{\mu_+}{h}\right)^2 (kI_{\mathrm{HC}} + B_{\mathrm{res}})^2}. \tag{4}$$

The notation for the fit function separates the variable from the parameters by a semicolon. The zero-field values ν_{HF} as obtained via this Breit-Rabi fit are plotted in Fig. 3d as the deviation from ν_{lit}.

E. Systematic tests

The following experimental arrangements and conditions have undergone changes for the 10 *sets* (summarised in the top part of table II). The beam velocity varied due to different settings of d_{s} and the temperature of the PTFE tubing. The first three *sets* operated with the straight PTFE tubing then the bent tubing was used. The need for an improved monitoring of I_{HC} and the advantage of a faster data acquisition scheme based on the total count rate instead of the lock-in amplifier signal became evident in a preliminary evaluation of the first three *sets* and motivated the additional changes at that stage. Two opening diameters for aperture 3, resulting in different beam sizes at the entrance of the cavity, were also investigated. This is of special interest as an even larger beam diameter is expected for the $\overline{\mathrm{H}}$ HFS spectroscopy. Additionally, the last 4 *sets* were performed with a second cavity of the same but slightly upgraded design. Three aspects were only changed for individual *sets*. For *set* 7 only one instead of two layers of magnetic shielding were used, for *set* 3 the superconducting sextupole worked with a larger magnetic field strength leading to a shorter focal length, and for *set* 4 the direction of the static magnetic field (Helmholtz coils) was not reversed.

The obtained results for ν_{HF} of the 10 *sets* by firstly fitting all *cycles* in a *set* using the fit function (10) and secondly the Breit-Rabi fit (4) are presented in Fig. 3d. Additionally the average reduced χ^2 of all fits to *cycles* within a *set* and the reduced χ^2 of the Breit-Rabi fit are given in table II. On the level of

the achieved statistical precision no significant dependence of the 10 results on any of the changed experimental conditions could be found. This justified to combine the 10 individual results into one weighted mean value. Our final result deviates from the literature value by $\nu_{\mathrm{HF}} - \nu_{\mathrm{lit}} = -3.4\,\mathrm{Hz}$ with a total uncertainty of $\sigma_{\mathrm{tot}} = 3.8\,\mathrm{Hz}$, which corresponds to a relative precision of 2.7 ppb. The mean value is shown in Fig. 3d as the dashed red line and the total 1σ uncertainties as the grey shaded area.

The fit parameters B_{osc}, $\bar{v}_H$ and σ_v, which were fixed to a common average value for each set, were varied in order to assess the potential systematic uncertainties originating from the fit procedure. The complete analysis was repeated 6 times with setting each of the three parameters individually to its lower and upper 1σ boundary. The observed shifts of ν_{HF} for each parameter are listed in table I. However, those three values added in quadrature yielded 0.06 Hz and present a negligible systematic uncertainty. The rubidium clock, which served as frequency standard, supplied a 10 MHz reference signal to the microwave synthesiser. A calibration was performed and revealed a shift of 11.4 mHz or equivalently 1.14 ppb. This corresponds to 1.6 Hz for ν_{HF} and is conservatively used as a 1σ systematic uncertainty. Table I summarises the error budget.

Table I. *Error budget*

contribution	1σ st.dev. (Hz)
systematic error	
frequency standard	1.62
common fit parameters	
$\bar{v}_H$	0.05
σ_v	0.03
B_{osc}	0.02
systematic error total	1.62
statistical error	3.43
total error	3.79

II. METHODS

A. Resonance line shape

The σ_1-transition in ground-state hydrogen is driven by an external microwave field, which is generated in a strip-line cavity and takes the form

$$\begin{aligned} \mathbf{B}_{\mathrm{osc}}(t) &= B_{\mathrm{osc}}\mathbf{e}_B \cos(\omega t)\cos(\omega_{\mathrm{cav}} t), \\ \omega_{\mathrm{cav}} &= \frac{\pi}{T_{\mathrm{int}}} = \frac{\pi v_H}{L_{\mathrm{cav}}}, \\ & 0 < t < T_{\mathrm{int}}, \end{aligned} \tag{5}$$

where $\mathbf{e}_B$ is the unit vector pointing in the direction of the magnetic field (z-axis in the frame of the atoms, x-axis in the coordinate system of the experiment) and $\nu = \omega/2\pi$ is the applied microwave frequency. The term $\cos(\omega_{cav} t)$ describes the changing amplitude of the magnetic field in the cavity along the beam propagation direction. T_{int} is the interaction time, which in turn follows from the hydrogen beam velocity v_H and the length of the cavity L_{cav}.

The small external magnetic field is aligned parallel to the oscillating magnetic field, which only for the σ_1-transition leads to non-vanishing matrix elements. In addition the Zeeman shift separates the ground-state hydrogen sub levels by more than the observed resonance width. Therefore, the transition dynamics is well described within the framework of the two-level system

$$\begin{aligned} |\phi\rangle &= c_1(t)|\phi_1\rangle + c_2(t)|\phi_2\rangle, \\ |\phi_1\rangle &= |F=0, M_F=0\rangle = \sqrt{1/2}\left(|\uparrow^e\downarrow_p\rangle - |\downarrow_e\uparrow^p\rangle\right), \\ |\phi_2\rangle &= |F=1, M_F=0\rangle = \sqrt{1/2}\left(|\uparrow^e\downarrow_p\rangle + |\downarrow_e\uparrow^p\rangle\right), \\ \hat{\mathcal{H}}_{\mathrm{atom}}|\phi_i\rangle &= E_i|\phi_i\rangle, \\ |c_1(t)|^2 + |c_2(t)|^2 &= 1. \end{aligned} \tag{6}$$

To obtain the time evolution of this system under the influence of the oscillating magnetic field the Hamiltonian needs to be extended by the interaction $\hat{\mathcal{H}}_{\mathrm{int}} = -\hat{\boldsymbol{\mu}} \cdot \mathbf{B}_{\mathbf{osc}}(t)$ with

$$\hat{\boldsymbol{\mu}} = -|g_e|\mu_B \frac{1}{\hbar}\hat{\mathbf{S}}^{\mathbf{e}} + g_p \mu_N \frac{1}{\hbar}\hat{\mathbf{S}}^{\mathbf{p}}, \tag{7}$$

for hydrogen. Here, $\hat{\mathbf{S}}^{\mathbf{i}}$ are the spin operators acting on the electron or proton spinor as indicated by the superscript. An analytical solution can be found for conventional Rabi experiments, where the oscillating (or rotating) magnetic field has a constant amplitude B_{osc} and doesn't include the term $\cos(\omega_{cav} t)$. If the system is initially prepared purely in state $|\phi_1\rangle$, then the conversion probability $|c_2|^2$ of finding it after a given interaction time T_{int} in the second state $|\phi_2\rangle$ depends on the strength of B_{osc} and the detuning $\Omega_{\mathrm{D}} = \omega - \omega_{12}$ with $\hbar\omega_{12} = E_2 - E_1$:

$$|c_2|^2 = \frac{\Omega_{\mathrm{R}}^2}{\Omega_{\mathrm{D}}^2 + \Omega_{\mathrm{R}}^2} \sin^2\left(\frac{1}{2}\sqrt{\Omega_{\mathrm{D}}^2 + \Omega_{\mathrm{R}}^2}\, T_{\mathrm{int}}\right), \tag{8}$$

where Ω_{R} is the Rabi frequency, which is proportional to the amplitude of the oscillating magnetic field. The relation for the σ_1-transition is

$$\Omega_{\mathrm{R}} = \underbrace{\left(|g_e|\mu_B + g_p\mu_N\right)}_{\mu_+} \frac{B_{\mathrm{osc}}}{2\hbar}. \tag{9}$$

Table II. ***Parameters of the data sets.*** *Comparison of the 10* sets. *The 4 blocks of rows summarize (i) experimental conditions, (ii) statistics of the data acquisition, (iii) average fit parameter of* cycles *and the average reduced chi-squares from applying fit-formula (11), and finally (iv) the fit parameters and the corresponding reduced chi-square from applying the Breit-Rabi fit (4).*

set	1	2	3	4	5	6	7	8	9	10
PTFE tubing	straight	straight	straight	90 deg.	90 deg.	90 deg.	90 deg.	90 deg.	90 deg.	90 deg.
cryostat temperature (K)	23	16	100	50	50	50	50	50	50	50
d_s (mm)	115	35	91	21	21	16	16	16	16	115
cavity	# 1	# 1	# 1	# 1	# 1	# 1	# 2	# 2	# 2	# 2
precise monitoring of I_{HC}	no	no	no	yes	yes	yes	yes	yes	yes	yes
supercond. sextupole (A)	350	350	400	350	350	350	350	350	350	350
beam diameter (mm)	8	8	8	8	8	8	8	8	22	22
shielding layers	2	2	2	2	2	2	1	2	2	2
I_{HC} polarity	$\pm$	$\pm$	$\pm$	+	$\pm$	$\pm$	$\pm$	$\pm$	$\pm$	$\pm$
number of *scans*	8	6	6	10	12	12	16	16	12	12
number of *cycles*	23	46	26	50	60	60	80	80	60	60
frequency data points	41	21	26	39	39	39	39	39	39	39
acqu. time / data point (s)	60	40	40	5	5	5	5	5	5	5
v (m/s)	1066 (1)	962 (2)	1152 (2)	888 (2)	857 (3)	883 (2)	933 (2)	922 (1)	1049 (1)	1131 (1)
σ_v (m/s)	152 (2)	145 (3)	156 (2)	160 (2)	184 (2)	139 (2)	124 (2)	129 (2)	183 (1)	149 (1)
B_{osc} (10^{-7} T)	6.86 (0.01)	6.49 (0.01)	8.14 (0.01)	5.73 (0.01)	5.81 (0.01)	5.78 (0.01)	6.70 (0.03)	6.28 (0.05)	6.54 (0.03)	6.93 (0.03)
R_0 (Hz)	27088 (232)	24420 (576)	26517 (234)	26998 (458)	20889 (237)	26118 (84)	23100 (194)	24825 (225)	56390 (2806)	31584 (1724)
ΔR (Hz)	891 (30)	476 (43)	1112 (29)	1471 (71)	795 (47)	1484 (50)	1126 (42)	1401 (51)	4499 (907)	3284 (154)
av. $\chi^2/n.d.f.$ of res. curves	2.6 (0.7)	1.6 (0.5)	1.9 (0.5)	1.2 (0.3)	1.0 (0.3)	1.2 (0.2)	1.1 (0.3)	1.1 (0.2)	1.9 (0.4)	1.9 (0.4)
B_{res} (10^{-7} T)	4.0 (1.0)	3.9 (2.6)	2.3 (2.0)	11.9 (19.1)	5.4 (1.9)	5.7 (1.0)	3.1 (1.3)	3.5 (1.1)	2.5 (0.5)	2.7 (0.5)
k (10^{-5} T/A)	45.83 (0.02)	45.47 (0.16)	45.70 (0.14)	45.87 (0.37)	45.76 (0.06)	45.80 (0.03)	45.85 (0.04)	45.90 (0.03)	45.90 (0.02)	45.89 (0.02)
$\chi^2/n.d.f.$ of Breit-Rabi fit	17.5/21	38.6/44	41.3/24	70.0/47	65.3/57	48.5/57	101.0/77	83.2/77	75.0/57	55.6/57
ν_{HF} - ν_{lit} (Hz)	−12.0 (10.6)	22.6 (22.2)	20.8 (19.4)	19.7 (46.7)	5.7 (23.9)	−9.2 (12.8)	7.1 (11.4)	−2.9 (9.2)	−8.8 (6.9)	−3.5 (6.4)

Including the term $\cos(\omega_{cav}t)$ requires numerical methods to determine the state-conversion probability. Figure 4 shows a comparison of $|c_2|^2$ as a function of the detuning Ω_D and the driving strength B_{osc} of conventional Rabi spectroscopy and the stripline cavity designed for the antihydrogen experiment. The latter case features the distinct *double-dip* structure with vanishing effects at the actual transition frequency. For a given interaction time T_{int} the best precision is achieved with the first full state conversion in both situations. For the conventional case this corresponds to a so-called π-pulse indicating that the condition $\Omega_R \cdot T_{int} = \pi$ is satisfied or alternatively $B_{osc} = h\mu_+^{-1}T_{int}^{-1}$. The *double-dip* resonance reaches the first full state conversion when applying a somewhat stronger oscillating magnetic field

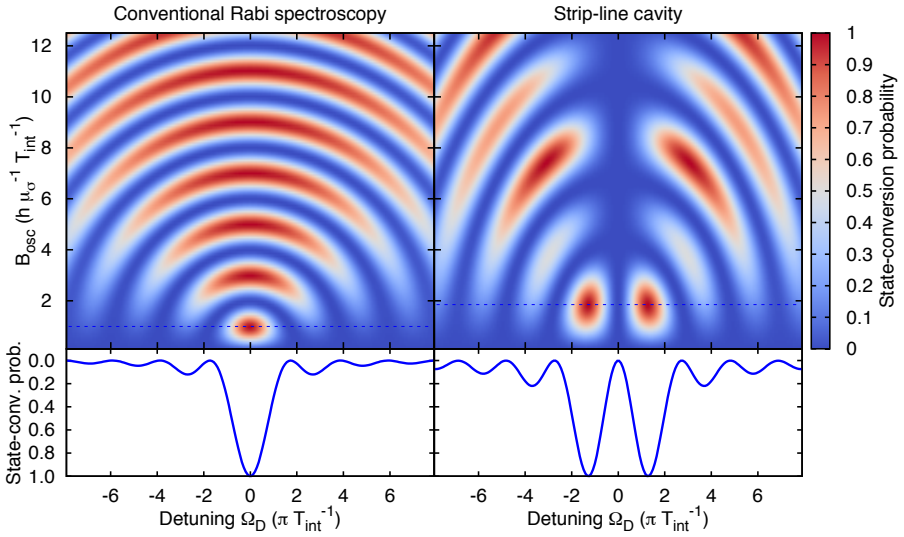

Figure 4. ***State-conversion probability maps for the detuning and driving strength.*** *Comparison of the state-conversion probabilities as a function of the detuning Ω_D (in units of πT_{int}^{-1}) and the amplitude of the oscillating magnetic field B_{osc} (in units of $h\mu_+^{-1}T_{int}^{-1}$) for the case of conventional Rabi spectroscopy (left) and when using a strip-line cavity (right) to drive the transition. Both cases refer to a mono-energetic beam, which translates to a fixed interaction time T_{int}. The dashed horizontal line indicates the required driving strength to reach the first complete state conversion. The plots below are projections of the state-conversion probabilities at the dashed lines and show the ideal (i.e. mono-energetic) line shapes observed as count rate drops in the Rabi experiments.*

$B_{\rm osc} \sim 1.86 \times h\mu_+^{-1}T_{\rm int}^{-1}$.

From a 2D-map as shown in Fig. 4 fit functions of the state-conversion probabilities for a mono-energetic beam can be derived with ν_c, the strength of $B_{\rm osc}$, and the hydrogen beam velocity v_H as fit parameters. This was realised by constructing a 2D-spline interpolation $\mathcal{S}(\nu;\nu_c,B_{\rm osc},v_H)$ to the numerically generated state-conversion probabilities at discrete points. A more realistic resonance line shape is then obtained by including the effect of the velocity distribution of the hydrogen beam, which translates to a not sharply defined interaction time $T_{\rm int}$. Note that both axis of the 2D-maps are normalised to $T_{\rm int}^{-1}$. Therefore, on an absolute scale for $\Omega_{\rm D}$ and $B_{\rm osc}$ a change of $T_{\rm int}$ is equivalent to a 2D-zooming of the state-conversion probability map. The roughly Gaussian velocity distribution of the hydrogen beam after passage of the polarising and velocity-selecting permanent sextupole magnets is approximated by binomial coefficients for a discrete numerical realisation of the convolution

$$\begin{aligned} \mathcal{F}(\nu;\nu_c,&B_{\rm osc},\bar{v}_H,\sigma_v) = \\ &= 2^{-N}\sum_{n=0}^{N}\binom{N}{n}\mathcal{S}(\nu;\nu_c,B_{\rm osc},v_{(N,n)}), \\ v_{(N,n)} &= \bar{v}_H + (n-N/2)dv, \\ dv &\sim 2\sigma_v N^{-1/2}. \end{aligned} \tag{10}$$

The result of a convolution with such a velocity distribution is illustrated in Fig. 5 and compared to a measured map. The present analysis used $N = 6$ because choices of $N > 6$ did not change nor improve the fit results. For completeness two more fit parameters were needed. In order to scale the state-conversion probability, which is a number between 0 and 1, to the observed count rates, a count rate baseline R_0 and a count rate drop for complete state conversion ΔR were introduced

$$\begin{aligned} \mathcal{F}_R(\nu;\nu_c,&B_{\rm osc},\bar{v}_H,\sigma_v,R_0,\Delta R) = \\ &= R_0 - \Delta R\cdot\mathcal{F}(\nu;\nu_c,B_{\rm osc},\bar{v}_H,\sigma_v), \end{aligned} \tag{11}$$

which are albeit not relevant for the obtained results.

III. ACKNOWLEDGEMENT

We want to thank H. Kundsen, H.-P. E. Kristiansen, F. Caspers, T. Kroyer, S. Federmann, P. Caradonna, M. Wolf, M. Heil, F. Pitters, C. Klaushofer, S. Friedreich, and B. Wünschek for their contributions. We acknowledge technical support by the CERN Cryolab and Instrumentation group TE-CRG-CI as well as the CERN Magnet Normal Conducting group TE-MSC-MNC.

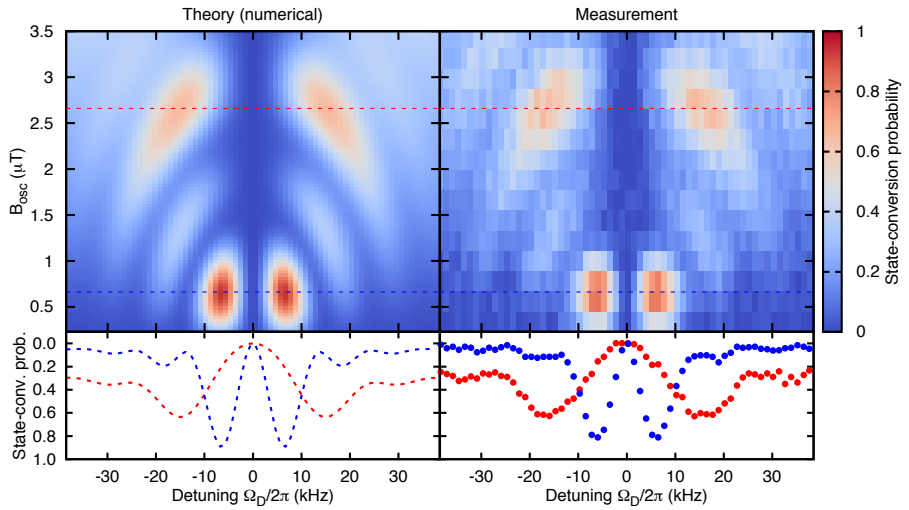

Figure 5. ***State-conversion probability maps convoluted with a velocity distribution.*** *Comparison of theoretical and measured state-conversion probabilities as a function of the detuning $\Omega_D/2\pi$ in units of kHz and the amplitude of the oscillating magnetic field B_{osc} in units of μT. The theoretical map includes the effect of a Gaussian-like velocity distribution with $\bar{v}_H$=1060 m/s and σ_v=95 m/s. The measurement was taken setting a large distance between the permanent sextupole magnets of d_s=115 mm as it has been used for the* sets *1 and 10. The blue and red dashed horizontal lines indicate the driving strengths, where the first and second full state conversion would be reached in the case of a mono energetic beam. The plots below are projections of the state-conversion probabilities at the dashed lines showing good agreement between theory and measurement. Frequency spectra across the narrow* double-dips *at the first state conversion yield the highest precision.*

This work has been supported by the European Research Council under European Union's Seventh Framework Programme (FP7/2007-2013)/ ERC Grant agreement (291242), the Austrian Ministry of Science and Research, the Austrian Science Fund (FWF): W1252-N27.

IV. AUTHOR CONTRIBUTIONS

M.D. prepared and performed the experiment, carried out the data analysis, and wrote parts of the initial manuscript. C.B.J. performed the experiment and carried out parts of the data analysis. B.K. and C.S. performed simulations. C.M. and M.C.S. prepared and performed the experiment, guided and carried out parts of the data analysis, and wrote the manuscript. O.M. and J.Z. prepared the experiment. E.W. proposed and prepared the experiment, guided the data analysis, and wrote the manuscript.

[1] Karshenboim, S. G. *et al.*, The Hydrogen Atom: Precision Physics of Simple Atomic Systems. vol. **570**, *Lecture Notes in Physics*. Springer-Verlag Berlin Heidelberg (2001).

[2] Mohr, P. J., Taylor, B. N. & Newell, D. B. CODATA recommended values of the fundamental physical constants: 2014. *Rev. Mod. Phys.* **88**, 035009 (2016).

[3] Parthey, C. G. *et al.*, Improved Measurement of the Hydrogen 1*S*-2*S* Transition Frequency. *Phys. Rev. Lett.* **107**, 203001 (2011).

[4] Hellwig, H. *et al.*, Measurement of the Unperturbed Hydrogen Hyperfine Transition Frequency. *IEEE Transactions on Instrumentation and Measurement* **19**, 200 (1970).

[5] Karshenboim, S. G. Some possibilities for laboratory searches for variations of fundamental constants. *Canadian Journal of Physics* **78**, 639 (2000).

[6] Essen, L. *et al.*, Frequency of the Hydrogen Maser. *Nature* **229**, 110 (1971).

[7] Essen, L. *et al.*, Hydrogen Maser Work at the National Physical Laboratory. *Metrologia* **9**, 128 (1973).

[8] Ramsey, N. F. Atomic hydrogen hyperfine structure experiments. in *Quantum Electrodynamics* T. Kinoshita (ed.), pp. 673–695. World Scientific, Singapore (1990).

[9] Ramsey, N. F. Experiments with separated oscillatory fields and hydrogen masers. *Rev. Mod. Phys.*

62, 541 (1990).
[10] Charlton, M. *et al.*, Antihydrogen physics. *Phys. Rep.* **241**, 65 (1994).
[11] Holzscheiter, M., Charlton, M. & Nieto, M. The route to ultra-low energy antihydrogen. *Phys. Rep.* **402**, 1 (2004).
[12] Hori, M. & Walz, J. Physics at CERN's Antiproton Decelerator. *Progress in Particle and Nuclear Physics* **72**, 206 (2013).
[13] Andresen, G. B. *et al.*, Trapped antihydrogen. *Nature* **468**, 673 (2010).
[14] Enomoto, Y. *et al.*, Synthesis of Cold Antihydrogen in a Cusp Trap. *Phys. Rev. Lett.* **105**, 243401 (2010).
[15] Gabrielse, G. *et al.*, Trapped Antihydrogen in Its Ground State. *Phys. Rev. Lett.* **108**, 113002 (2012).
[16] Kuroda, N. *et al.*, A source of antihydrogen for in-flight hyperfine spectroscopy. *Nat. Commun.* **5**, 4089 (2014).
[17] Perez, P., Sacquin, Y. The GBAR experiment: gravitational behaviour of antihydrogen at rest. *Classical and Quantum Gravity* **29**, 184008 (2012).
[18] Aghion, S. *et al.*, A moiré deflectometer for antimatter. *Nat. Commun.* **5**, 5538 (2014).
[19] Amole, C. *et al.*, An experimental limit on the charge of antihydrogen. *Nat. Commun.* **5**, 4955 (2014).
[20] Ahmadi, M. *et al.*, An improved limit on the charge of antihydrogen from stochastic acceleration. *Nature* **529**, 373 (2016).
[21] Ulmer, S. *et al.*, High-precision comparison of the antiproton-to-proton charge-to-mass ratio. *Nature* **524**, 196 (2015).
[22] DiSciacca, J. *et al.*, One-Particle Measurement of the Antiproton Magnetic Moment. *Phys. Rev. Lett.* **110**, 130801 (2013).
[23] Bluhm, R., Kostelecký, V. A. & Russell, N. CPT and Lorentz Tests in Hydrogen and Antihydrogen. *Phys. Rev. Lett.* **82**, 2254 (1999).
[24] Kostelecký, V. A. & Vargas, A. J. Lorentz and CPT tests with hydrogen, antihydrogen, and related systems. *Phys. Rev. D* **92**, 056002 (2015).
[25] Widmann, E. *et al.*, Measurement of the hyperfine structure of antihydrogen in a beam. *Hyperfine Interact.* **215**, 1 (2013),
[26] Mohri, A. & Yamazaki, Y. A possible new scheme to synthesize antihydrogen and to prepare a polarised antihydrogen beam. *Europhys. Lett.* **63**, 207 (2003).
[27] Widmann, E. *et al.* Hyperfine structure measurements of antiprotonic helium and antihydrogen. in *The Hydrogen Atom: Precision Physics of Simple Atomic Systems* Karshenboim, S. G., Pavone, F. S., Bassani, F., Inguscio, M. & Hänsch, T. W. (eds.) *Lecture Notes in Physics* vol. **570**, pp. 528–542. Springer-Verlag Berlin Heidelberg (2001),
[28] Amole, C. *et al.*, Resonant quantum transitions in trapped antihydrogen atoms. *Nature* **483**, 439 (2012).
[29] Rabi, I. I. *et al.*, A New Method of Measuring Nuclear Magnetic Moment. *Phys. Rev.* **53**, 318 (1938).
[30] Rabi, I. I., *et al.*, The Molecular Beam Resonance Method for Measuring Nuclear Magnetic Moments. The Magnetic Moments of $_3Li^6$, $_3Li^7$ and $_9F^{19}$. *Phys. Rev.* **55**, 526 (1939).
[31] Ramsey, N. Molecular beams. *Oxford University Press*, 2014 edn. (1986).
[32] Nafe, J. E. & Nelson, E. B. The Hyperfine Structure of Hydrogen and Deuterium. *Phys. Rev.* **73**, 718 (1948).
[33] Prodell, A. G. & Kusch, P. The Hyperfine Structure of Hydrogen and Deuterium. *Phys. Rev.* **88**, 184 (1952).
[34] Kusch, P. Redetermination of the Hyperfine Splittings of Hydrogen and Deuterium in the Ground State. *Phys. Rev.* **100**, 1188 (1955).
[35] McCullough, R. W. *et al.*, A new microwave discharge source for reactive atom beams. *Meas. Sci. Technol.* **4**, 79 (1993).
[36] Walraven, J. T. M. & Silvera, I. F. Helium-temperature beam source of atomic hydrogen. *Rev. Sci. Instrum.* **53**, 1167 (1982).
[37] Thonet, P. A. Use of Permanent Magnets in Multiple Projects at CERN. *IEEE Transactions on Applied Superconductivity* **26**, 4 (2016).
[38] Kroyer, T. Design of a Spin-Flip Cavity for the Measurement of the Antihydrogen Hyperfine Structure. *Tech. Rep. CERN-AB-Note-2008-016*, CERN, Geneva (2008).
[39] Federmann, S. A Spin-Flip Cavity for Microwave Spectroscopy of Antihydrogen. *dissertation*, Universität Wien. Fakultät für Physik (2012).
[40] Breit, G. & Rabi, I. I. Measurement of Nuclear Spin. *Phys. Rev.* **38**, 2082 (1931).